nature geoscience

SUPPLEMENTARY INFORMATION
https://doi.org/10.1038/s41561-018-0105-9

In the format provided by the authors and unedited.

Earth's oldest stable crust in the Pilbara Craton formed by cyclic gravitational overturns

Daniel Wiemer[1,2*], Christoph E. Schrank[1,2], David T. Murphy[1], Lana Wenham[1] and Charlotte M. Allen[1]

[1]Queensland University of Technology, Brisbane, Queensland, Australia. [2]University of Western Australia, Crawley, Western Australia, Australia.
*e-mail: daniel.wiemer@uwa.edu.au

Earth's oldest stable crust in the Pilbara craton formed by cyclic gravitational overturns

Supplementary Information

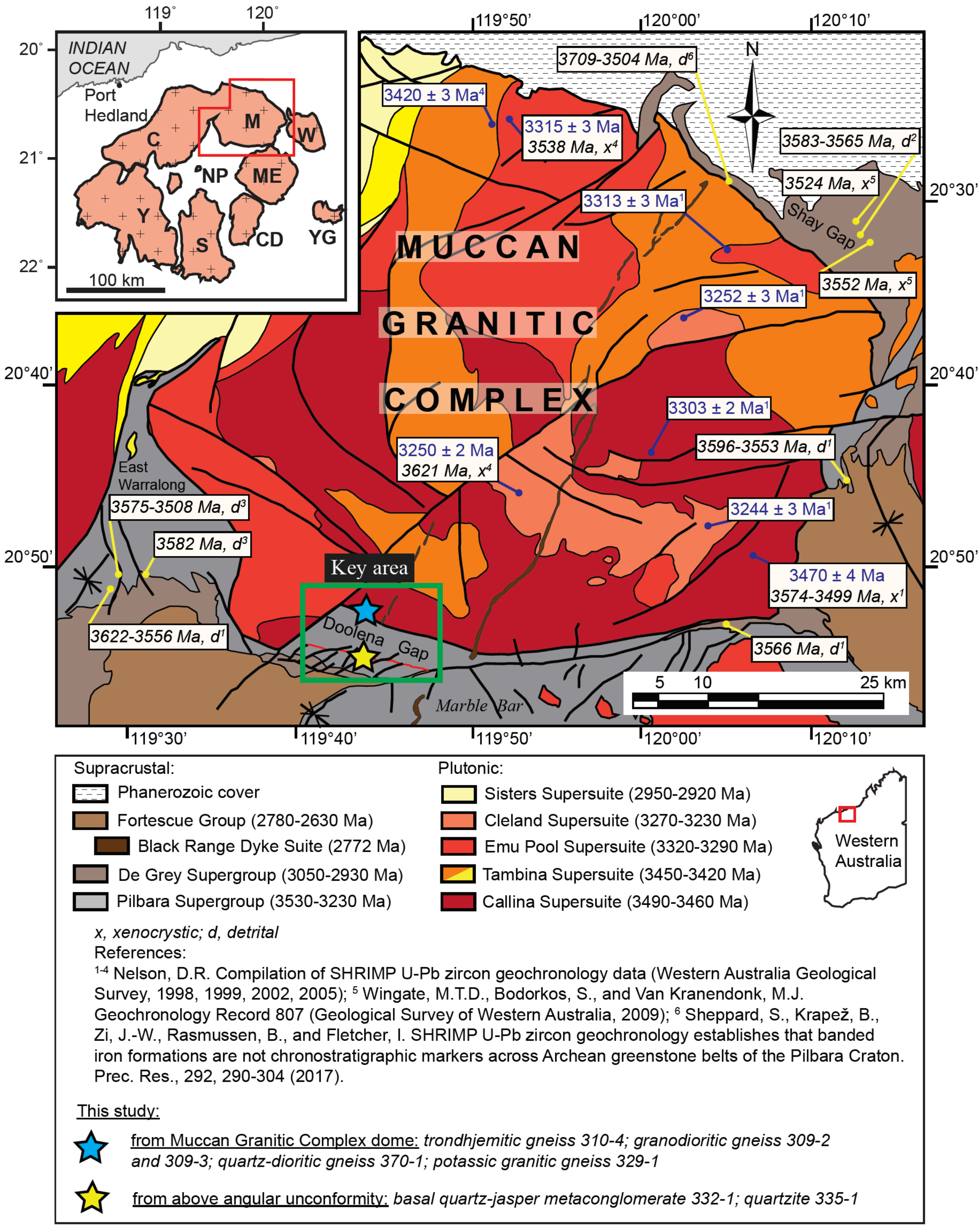

Supplementary Figure 1 | Simplified geological map of the Muccan Granitic Complex and surrounding greenstone belts. The position of the Muccan Granitic Complex and other granitic domes of the EPT are shown in the map, upper left corner, and the position of the EPT within Western Australia is shown in the image in the legend. Previous geochronological data include: U-Pb SHRIMP zircon upper intercept emplacement ages of dome components (blue), and $^{206}Pb/^{207}Pb$ SHRIMP age ranges of xenocrystic (x) and detrital (d) zircons ≥3500 Ma (black, italic). This study: locations of samples from the southwestern margin of the Muccan Granitic Complex and from metasedimentary rocks above the angular unconformity in the southerly adjacent Doolena Gap greenstone belt within the studied key area (rectangle) are shown (stars). Abbreviations for granitic complexes are: C, Carlindi; CD, Corruna Downs; M, Muccan; ME, Mount Edgar; NP, North Pole; S, Shaw; W, Warrawagine; Y, Yule; YG, Yilgalong

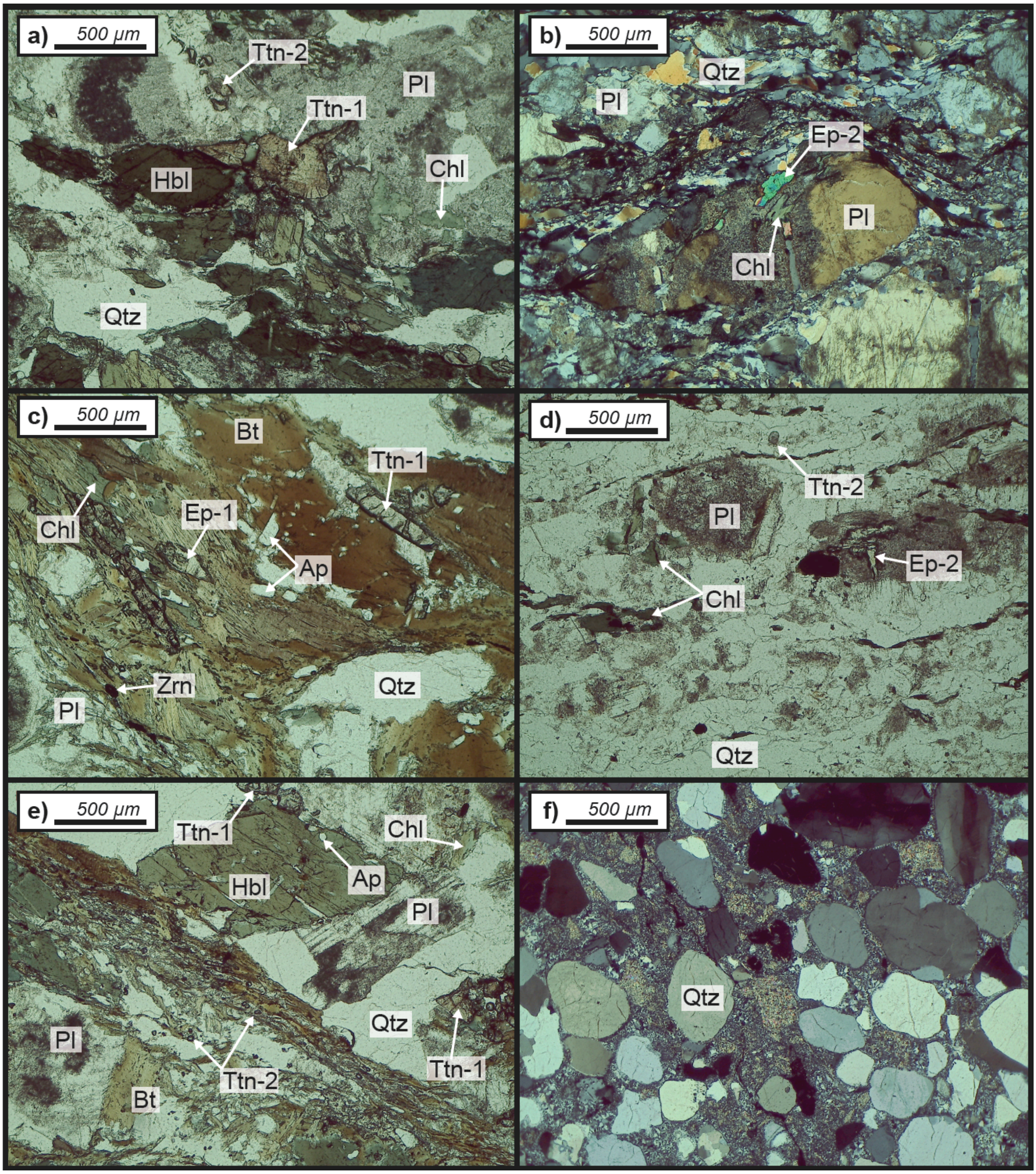

Supplementary Figure 2 | Representative petrographic images and sample descriptions. a, plane-polarised light image of granodioritic gneiss 309-2 (20°52'28.92" S/119°43'54.32 E) displaying a primary magmatic assemblage of coarse-grained, euhedral to subhedral hornblende, plagioclase and titanite (Ttn-1); interstitial quartz is recrystallised, and chlorite replaces plagioclase; a fine-grained, anhedral, metamorphic population of titanite (Ttn-2) is observed in association with chlorite and recrystallised (clear, albitic) margins of plagioclase. **b,** cross-polarised light image of trondhjemitic gneiss 310-4 (20°52’37.86” S/119°43’46.31” E) showing coarse-grained, anhedral, primary magmatic plagioclase porphyroclasts, which are partly retrogressed to epidote (Ep-2), chlorite and microliths of albite, alkali-feldspar and mica (dark cores); primary porphyroclasts are surrounded by S_2-deformation bands defined by recrystallised plagioclase and quartz, and laths of chlorite. note that the section is ~40µm thick, resulting in up to first order yellow interference colours in quartz. **c,** plane-polarised light image of quartz-dioritic gneiss 370-1 (20°52’31.98” S/119°43’56.67” E) displaying a primary magmatic assemblage of plagioclase, epidote (Ep-1), titanite (Ttn-1), apatite, biotite and accessory zircon. Biotite laths are aligned, defining the S_2-foliation, and are partly replaced by chlorite; interstitial quartz is fully recrystallised. **d,** plane-polarised light image of potassic granitic gneiss 329-1 (20°52’49.23” S/119°44’47.28 E) showing coarse-grained plagioclase porphyroclasts with altered magmatic cores (dark) and recrystallised albitic margins (clear); retrograde epidote and chlorite replace plagioclase cores and/or are observed in association with the recrystallised albitic margins of plagioclase; chlorite is also found as S_2-foliation-defining laths replacing former biotite in the matrix that comprises medium-grained remnants of primary plagioclase porphyroclasts, recrystallised quartz, albite and minor alkali-feldspar, and fine-grained, anhedral, metamorphic titanite (Ttn-2). **e,** plane-polarised light image of quartz-dioritic gneiss 370-1 displaying magmatic domains (upper right of image) of primary, coarse-grained, eu- to subhedral hornblende, plagioclase and titanite (Ttn-1), surrounded by recrystallised, interstitial quartz; the magmatic domain is cut by a S_2-deformation band of aligned, medium-grained, anhedral hornblende, biotite laths that are partly replaced by chlorite, and dynamically recrystallised quartz; metamorphic titanite (Ttn-2) appears as fine-grained, anhedral crystals throughout the deformation band. **f,** cross-polarised light image of quartzite/metasandstone 335-1 (20°55’20.04” S/119°44’21.11 E) from above the angular unconformity, demonstrating the un-deformed nature of the rock that escaped the D_2 RTI event.

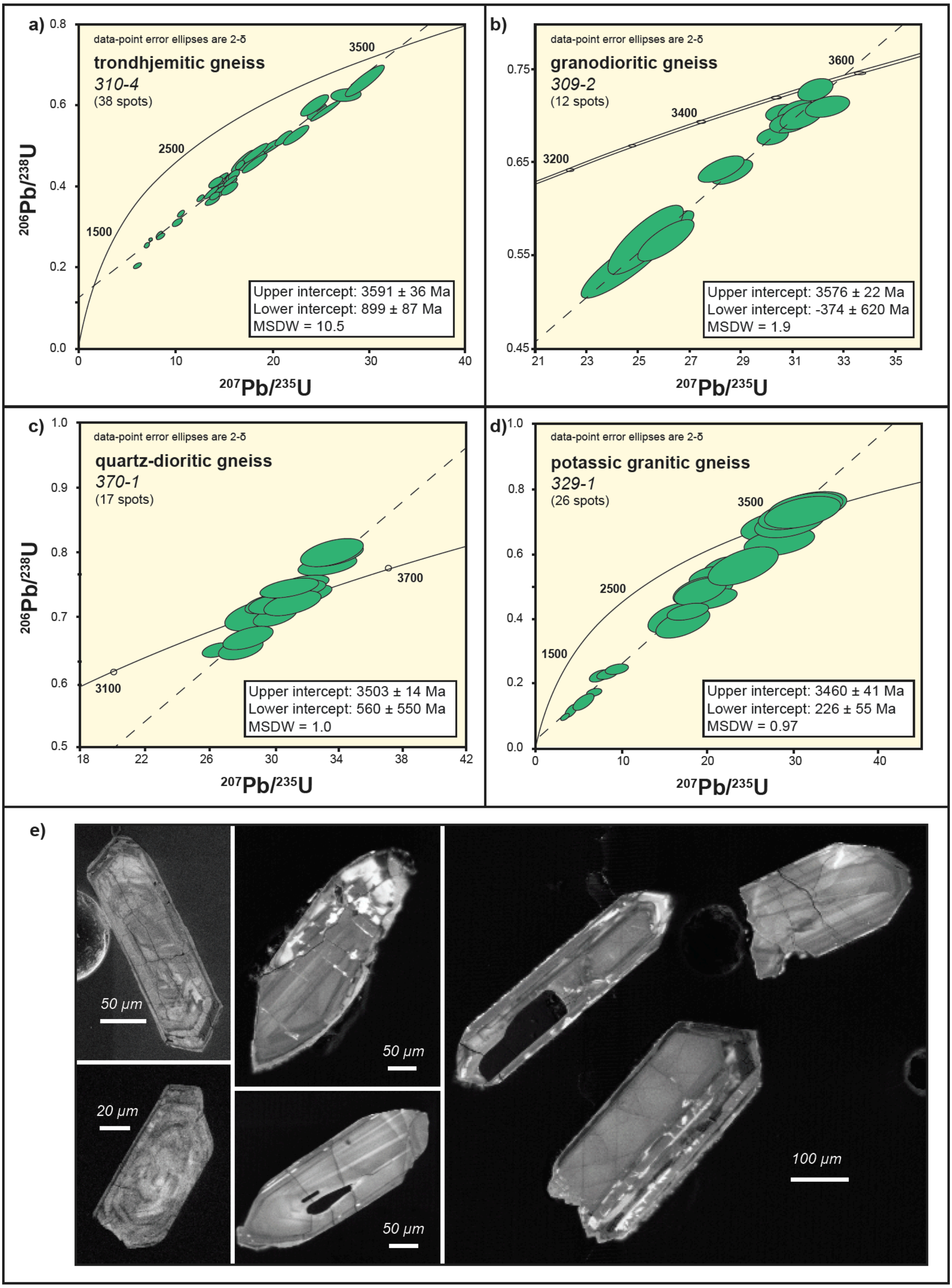

a)
data-point error ellipses are 2-σ
trondhjemitic gneiss
310-4
(38 spots)
Upper intercept: 3591 ± 36 Ma
Lower intercept: 899 ± 87 Ma
MSDW = 10.5
b)
data-point error ellipses are 2-σ
granodioritic gneiss
309-2
(12 spots)
Upper intercept: 3576 ± 22 Ma
Lower intercept: -374 ± 620 Ma
MSDW = 1.9
c)
data-point error ellipses are 2-σ
quartz-dioritic gneiss
370-1
(17 spots)
Upper intercept: 3503 ± 14 Ma
Lower intercept: 560 ± 550 Ma
MSDW = 1.0
d)
data-point error ellipses are 2-σ
potassic granitic gneiss
329-1
(26 spots)
Upper intercept: 3460 ± 41 Ma
Lower intercept: 226 ± 55 Ma
MSDW = 0.97
206Pb/238U
207Pb/235U
e)
50 µm
20 µm
50 µm
50 µm
100 µm

Supplementary Figure 3 | U-Pb LA-ICP-MS zircon Concordia diagrams and representative CL images of zircon from the Muccan Granitic Complex gneisses. **a**, trondhjemitic gneiss 310-4. **b**, granodioritic gneiss 309-2. **c**, quartz-dioritic gneiss 370-1. **d**, potassic granitic gneiss 329-1. Upper intercept ages are interpreted as the timing of zircon crystallisation and magmatic emplacement of the protoliths of the gneisses. Lower intercepts indicate Pb loss in the late Proterozoic-Phanerozoic. **e**, representative CL images of zircon displaying magmatic, concentric-oscillatory growth zoning; upper and lower left-panel images from potassic granitic gneiss 329-1, upper and lower mid-panel and right-panel images from quartz-dioritic gneiss 370-1; LA-ICP-MS analytical spots were focused on zircon interiors, avoiding marginal zones and fractures.

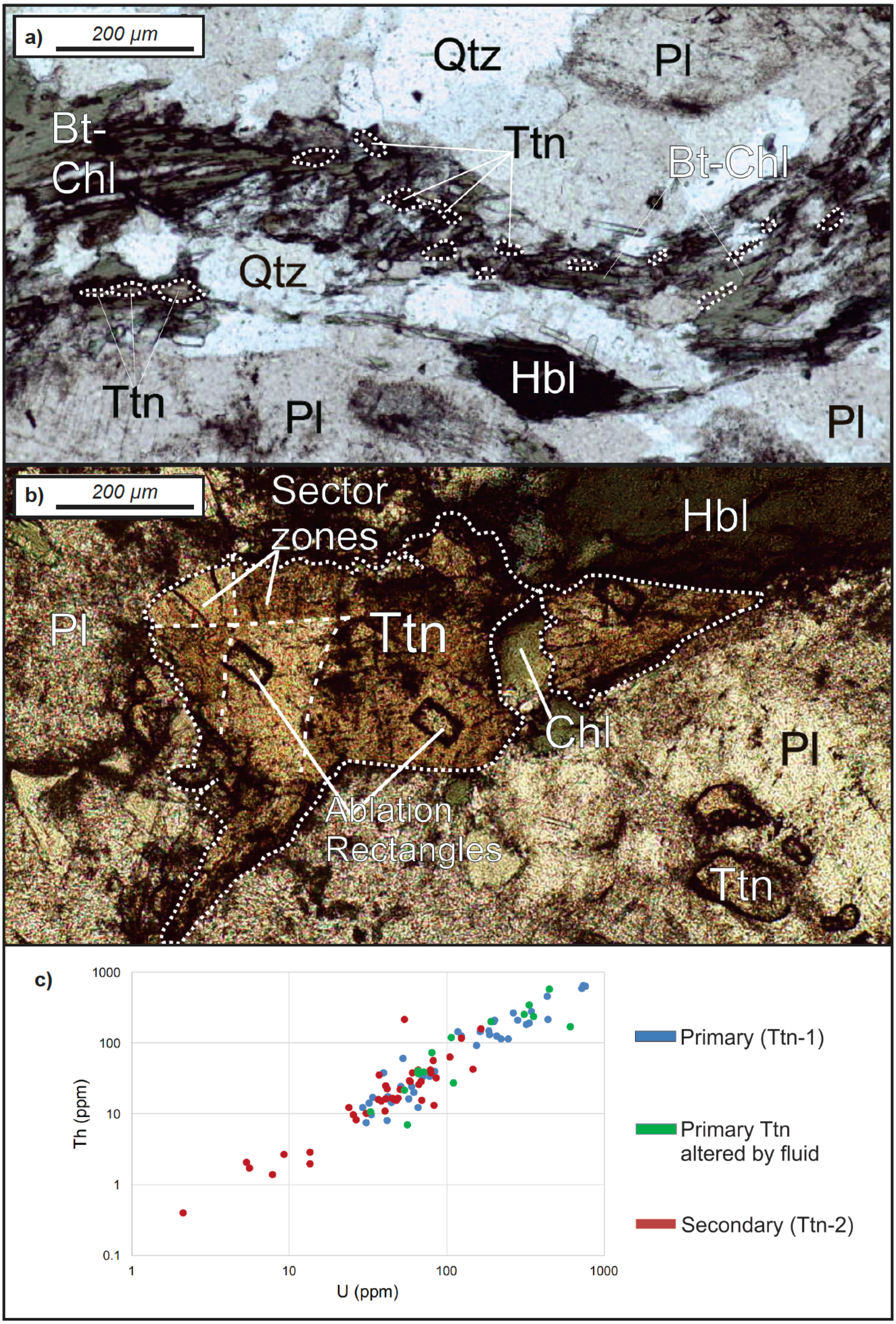

a)
200 µm
Qtz
Pl
Bt-
Chl
Ttn
Bt-Chl
Qtz
Hbl
Ttn
Pl
Pl
b)
200 µm
Sector
zones
Hbl
Pl
Ttn
Chl
Pl
Ablation
Rectangles
Ttn
c)
1000
100
10
1
0.1
Th (ppm)
1
10
100
1000
U (ppm)
Primary (Ttn-1)
Primary Ttn
altered by fluid
Secondary (Ttn-2)

Supplementary Figure 4 | Representative petrographic images of textural relationships and chemical U-Pb plot of primary and secondary titanite populations. a, plane-polarised light image of granodioritic gneiss 309-3 showing fine-grained, anhedral titanite in association with chlorite (replacing biotite), recrystallised quartz, and recrystallised albitic margins of primary plagioclase porphyroclasts within a D_2 syn-kinematic deformation band. **b,** plane-polarised light image of granodioritic gneiss 309-2 (detail of Supplementary Fig. 2a) displaying coarse-grained, eu- to subhedral primary titanite in association with magmatic plagioclase and hornblende. **c,** Th (ppm) vs. U (ppm) chemical plot demonstrating relatively low Th and U concentrations in secondary titanite (Ttn-2), whereas Th and U in primary titanite (Ttn-1) extend to higher concentrations and display a wider range of values at similar Th/U.

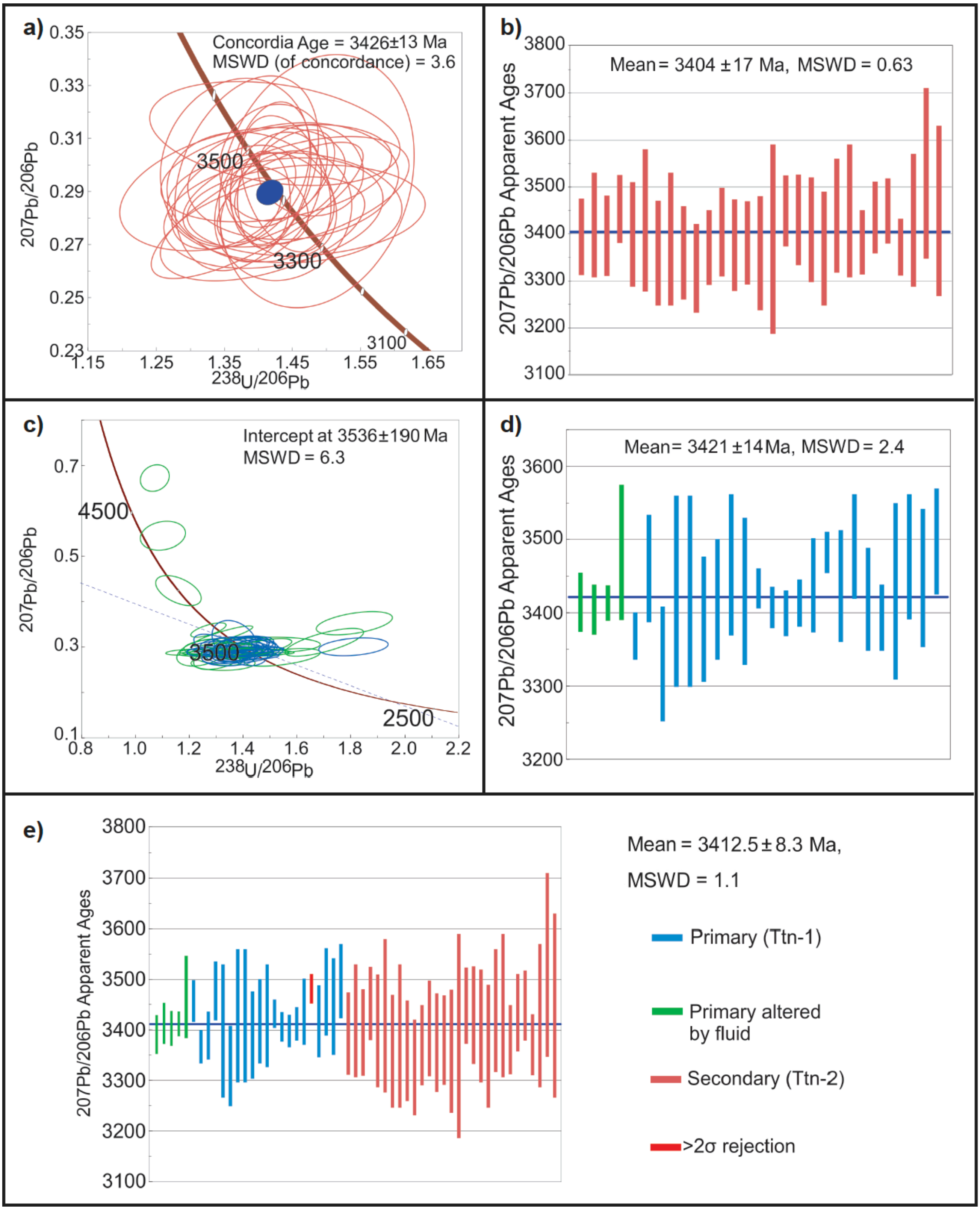

Supplementary Figure 5 | In-situ U-Pb LA-ICP-MS Terra-Wasserburg Concordia diagrams of primary and secondary titanite from granodioritic gneisses 309-2 and 309-3. a, Terra-Wasserburg Concordia plot of secondary titanite Ttn-2 displaying concordant U-Pb systematics with a Concordia age of 3426 ± 13 Ma. **b,** $^{207}Pb/^{206}Pb$ spot apparent ages of <4% discordance, yielding a weighted mean of 3404 ± 17 Ma for Ttn-2. **c,** Terra-Wasserburg Concordia plot of primary and fluid altered primary titanite Ttn-1 with a combined Concordia age of 3536 ± 190 Ma. **d,** $^{207}Pb/^{206}Pb$ spot apparent ages of <4% discordance, yielding a weighted mean of 3421 ± 14 Ma for primary and fluid altered primary titanite. **e,** $^{207}Pb/^{206}Pb$ spot apparent ages of <4% discordance, yielding a weighted mean of 3413 ± 8 Ma for the combined titanite populations. All error bars and ellipses are 2-sigma.

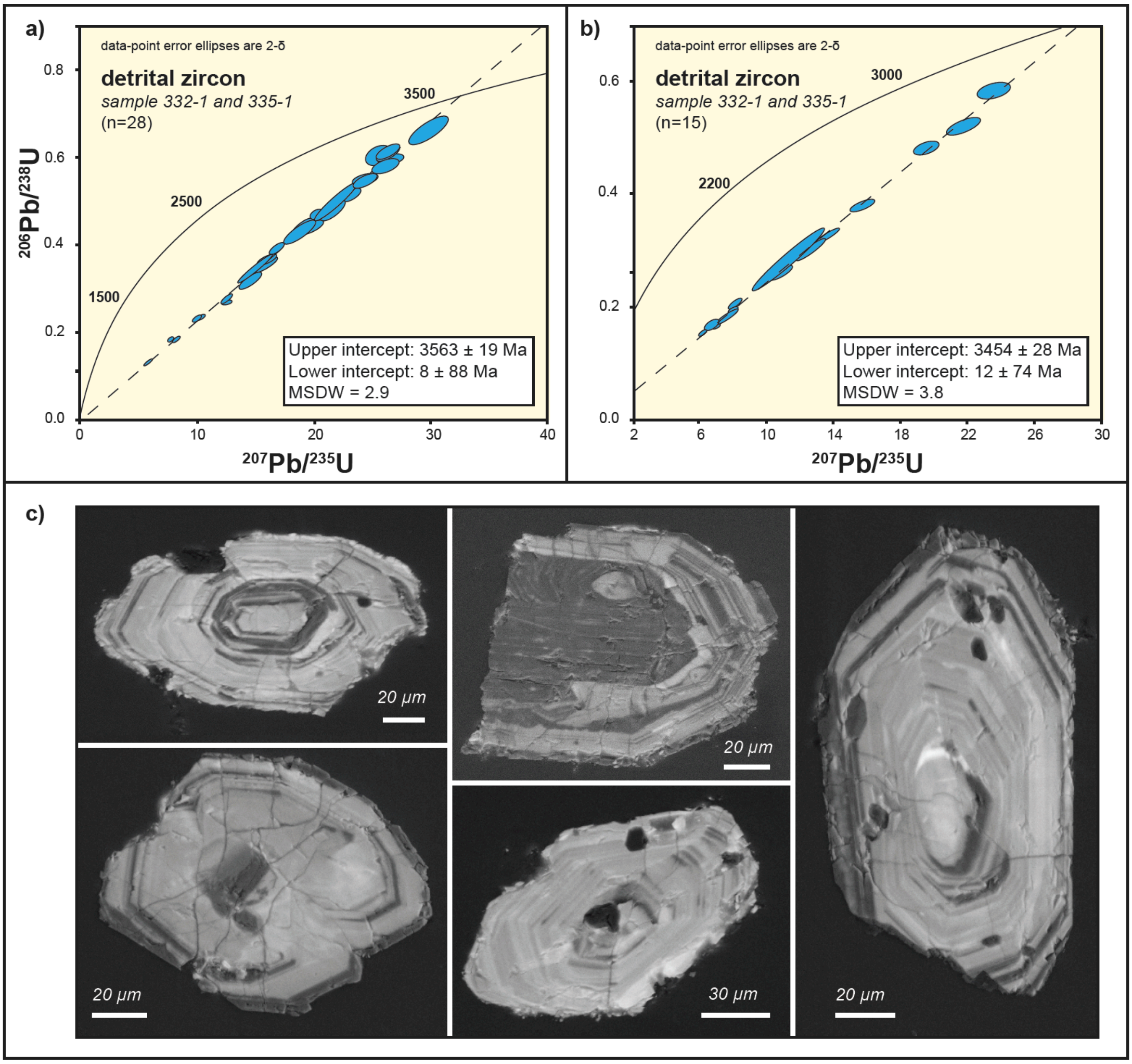

Supplementary Figure 6 | U-Pb zircon Concordia diagrams and representative CL images of detrital zircons from above the angular unconformity. The detrital zircons come from a basal quartz-jasper metaconglomerate (332-1) and a quartzite (335-1). **a**, 28 spots of old $^{207}Pb/^{206}Pb$ apparent ages yield a weighted mean of 3538 ± 32 Ma, or a relatively well-defined Discordia with an upper intercept of 3563 ± 19 Ma. **b**, 15 spots of relatively younger $^{207}Pb/^{206}Pb$ apparent ages yields a weighted mean of 3430 ± 20 Ma, or an upper intercept of 3454 ± 28 Ma. **c,** representative CL images reveal concentric-oscillatory growth zoning of the detrital zircon populations, indicating a magmatic origin.

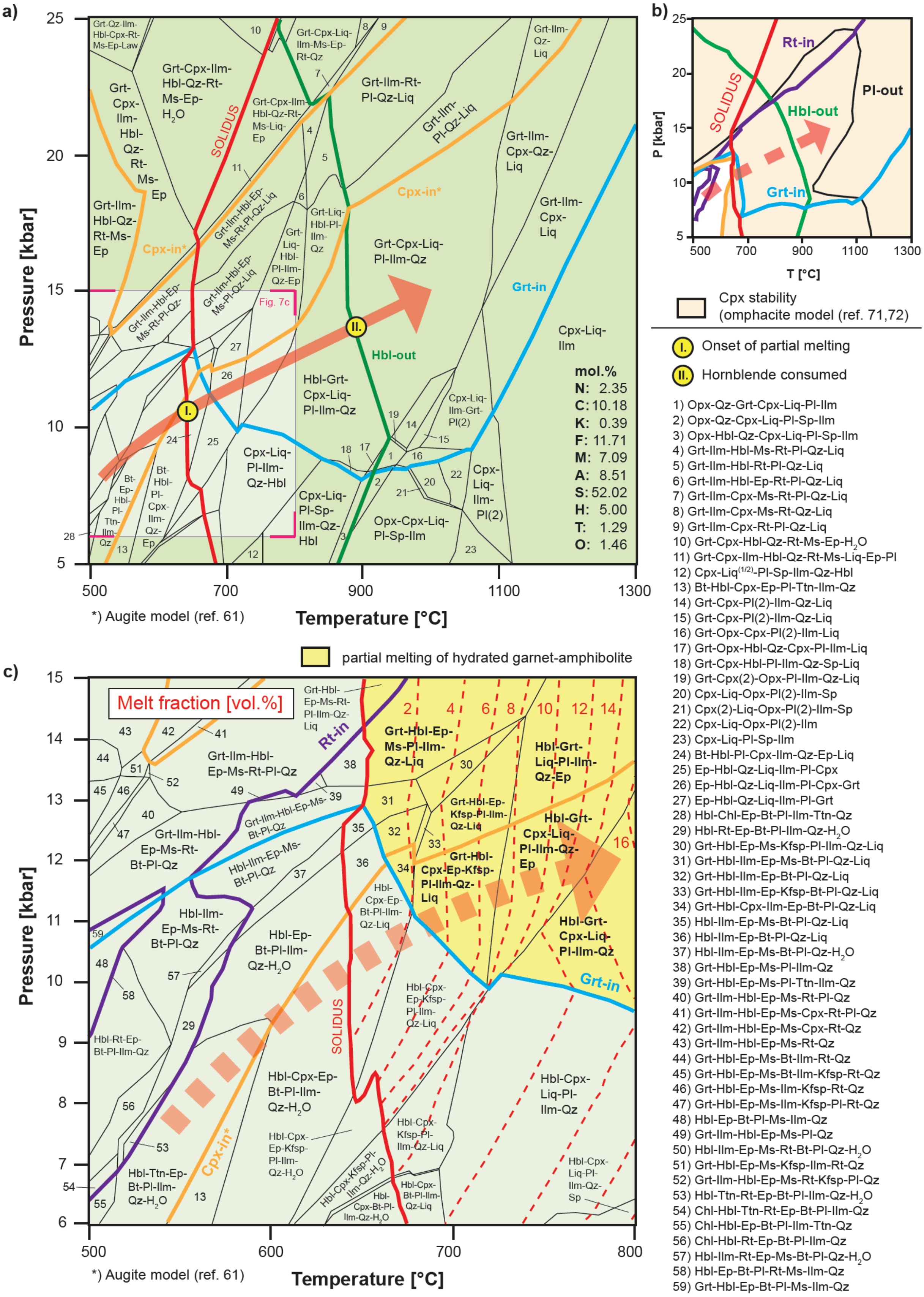
a)
Pressure [kbar]
Temperature [°C]
SOLIDUS
Cpx-in*
Hbl-out
Grt-in
Fig. 7c
mol.%
N: 2.35
C: 10.18
K: 0.39
F: 11.71
M: 7.09
A: 8.51
S: 52.02
H: 5.00
T: 1.29
O: 1.46
*) Augite model (ref. 61)
b)
P [kbar]
T [°C]
Rt-in
Pl-out
Hbl-out
Grt-in
Cpx stability (omphacite model (ref. 71,72)
I. Onset of partial melting
II. Hornblende consumed
1) Opx-Qz-Grt-Cpx-Liq-Pl-Ilm
2) Opx-Qz-Cpx-Liq-Pl-Sp-Ilm
3) Opx-Hbl-Qz-Cpx-Liq-Pl-Sp-Ilm
4) Grt-Ilm-Hbl-Ms-Rt-Pl-Qz-Liq
5) Grt-Ilm-Hbl-Rt-Pl-Qz-Liq
6) Grt-Ilm-Hbl-Ep-Rt-Pl-Qz-Liq
7) Grt-Ilm-Cpx-Ms-Rt-Pl-Qz-Liq
8) Grt-Ilm-Cpx-Ms-Rt-Qz-Liq
9) Grt-Ilm-Cpx-Rt-Pl-Qz-Liq
10) Grt-Cpx-Hbl-Qz-Rt-Ms-Ep-H_2O
11) Grt-Cpx-Ilm-Hbl-Qz-Rt-Ms-Liq-Ep-Pl
12) Cpx-Liq(1/2)-Pl-Sp-Ilm-Qz-Hbl
13) Bt-Hbl-Cpx-Ep-Pl-Ttn-Ilm-Qz
14) Grt-Cpx-Pl(2)-Ilm-Qz-Liq
15) Grt-Cpx-Pl(2)-Ilm-Qz-Liq
16) Grt-Opx-Cpx-Pl(2)-Ilm-Liq
17) Grt-Opx-Hbl-Qz-Cpx-Pl-Ilm-Liq
18) Grt-Cpx-Hbl-Pl-Ilm-Qz-Sp-Liq
19) Grt-Cpx(2)-Opx-Pl-Ilm-Qz-Liq
20) Cpx-Liq-Opx-Pl(2)-Ilm-Sp
21) Cpx(2)-Liq-Opx-Pl(2)-Ilm-Sp
22) Cpx-Liq-Opx-Pl(2)-Ilm
23) Cpx-Liq-Pl-Sp-Ilm
24) Bt-Hbl-Pl-Cpx-Ilm-Qz-Ep-Liq
25) Ep-Hbl-Qz-Liq-Ilm-Pl-Cpx
26) Ep-Hbl-Qz-Liq-Ilm-Pl-Cpx-Grt
27) Ep-Hbl-Qz-Liq-Ilm-Pl-Grt
28) Hbl-Chl-Ep-Bt-Pl-Ilm-Ttn-Qz
29) Hbl-Rt-Ep-Bt-Pl-Ilm-Qz-H_2O
30) Grt-Hbl-Ep-Ms-Kfsp-Pl-Ilm-Qz-Liq
31) Grt-Hbl-Ilm-Ep-Ms-Bt-Pl-Qz-Liq
32) Grt-Hbl-Ilm-Ep-Bt-Pl-Qz-Liq
33) Grt-Hbl-Ilm-Ep-Kfsp-Bt-Pl-Qz-Liq
34) Grt-Hbl-Cpx-Ilm-Ep-Bt-Pl-Qz-Liq
35) Hbl-Ilm-Ep-Ms-Bt-Pl-Qz-Liq
36) Hbl-Ilm-Ep-Bt-Pl-Qz-Liq
37) Hbl-Ilm-Ep-Ms-Bt-Pl-Qz-H_2O
38) Grt-Hbl-Ep-Ms-Pl-Ilm-Qz
39) Grt-Hbl-Ep-Ms-Pl-Ttn-Ilm-Qz
40) Grt-Ilm-Hbl-Ep-Ms-Rt-Pl-Qz
41) Grt-Ilm-Hbl-Ep-Ms-Cpx-Rt-Pl-Qz
42) Grt-Ilm-Hbl-Ep-Ms-Cpx-Rt-Qz
43) Grt-Ilm-Hbl-Ep-Ms-Rt-Qz
44) Grt-Hbl-Ep-Ms-Bt-Ilm-Rt-Qz
45) Grt-Hbl-Ep-Ms-Bt-Ilm-Kfsp-Rt-Qz
46) Grt-Hbl-Ep-Ms-Ilm-Kfsp-Rt-Qz
47) Grt-Hbl-Ep-Ms-Ilm-Kfsp-Pl-Rt-Qz
48) Hbl-Ep-Bt-Pl-Ms-Ilm-Qz
49) Grt-Ilm-Hbl-Ep-Ms-Pl-Qz
50) Hbl-Ilm-Ep-Ms-Rt-Bt-Pl-Qz-H_2O
51) Grt-Hbl-Ep-Ms-Kfsp-Ilm-Rt-Qz
52) Grt-Ilm-Hbl-Ep-Ms-Rt-Kfsp-Pl-Qz
53) Hbl-Ttn-Rt-Ep-Bt-Pl-Ilm-Qz-H_2O
54) Chl-Hbl-Ttn-Rt-Ep-Bt-Pl-Ilm-Qz
55) Chl-Hbl-Ep-Bt-Pl-Ilm-Ttn-Qz
56) Chl-Hbl-Rt-Ep-Bt-Pl-Ilm-Qz
57) Hbl-Ilm-Rt-Ep-Ms-Bt-Pl-Qz-H_2O
58) Hbl-Ep-Bt-Pl-Rt-Ms-Ilm-Qz
59) Grt-Hbl-Ep-Bt-Pl-Ms-Ilm-Qz
c)
partial melting of hydrated garnet-amphibolite
Melt fraction [vol.%]
Rt-in
Grt-in
Cpx-in*
SOLIDUS
*) Augite model (ref. 61)

Supplementary Figure 7 | P-T pseudosections of a putative TTG-source early Archaean metabasalt. P-T pseudosections of equilibrium mineral assemblages were computed with the Gibbs free-energy minimization software PerpleX for the average C-F2 metabasalt in the model system Na_2O-CaO-K_2O-FeO-MgO-Al_2O_3-SiO_2-H_2O-TiO_2-Fe_2O_3 (Methods). **a,** pseudosection of mid- to lower crustal P-T space, using the augite a-x relation model (ref. 61). In combination with our geochemical trace element modelling (Supplementary Fig. 9a), a P-T partial melting path (orange arrow) along an apparent thermal gradient of ca. 24°C km^{-1} is inferred within the stability field of garnet, but below the lower-pressure stability-limit of rutile (i.e., ca. 15kbar; Methods). The primary mode of partial melt generation is through de-hydration melting of hornblende of a garnet-amphibolite (garnet-hornblende-clinopyroxene-plagioclase-ilmenite-quartz ± epidote ± biotite). P-T conditions of ca. 10-15kbar and 680-900°C can be inferred for the generation of tonalitic partial melt, where the modal melt fraction reaches 25% at ca. 850-900°C. The computed solid residue comprises garnet-clinopyroxene-plagioclase-ilmenite-quartz (i.e., garnet-pyroxenite). **b,** simplified P-T pseudosection of the same bulk-rock composition, using the omphacite a-x model (ref. 71,72), in order to demonstrate the stability of clinopyroxene within low-T, high-P regions (light orange shading), where the augite model, as indicated by the absence of clinopyroxene in pseudosection (a), is not stabilised. **c,** detail of (a) showing equilibrium phase assemblages in the vicinity of the solidus and computed modal fractions of tonalitic partial melt. Bt, biotite; Cpx, clinopyroxene; Ep, epidote; Grt, garnet; Hbl, hornblende; Ilm, ilmenite; Kfsp, alkali-feldspar; Law, lawsonite; Liq, tonalitic partial melt; Ms, mica (muscovite-paragonite); Opx, orthopyroxene; Pl, plagioclase; Qz, quartz; Rt, rutile; Sp, spinel; Ttn, titanite.

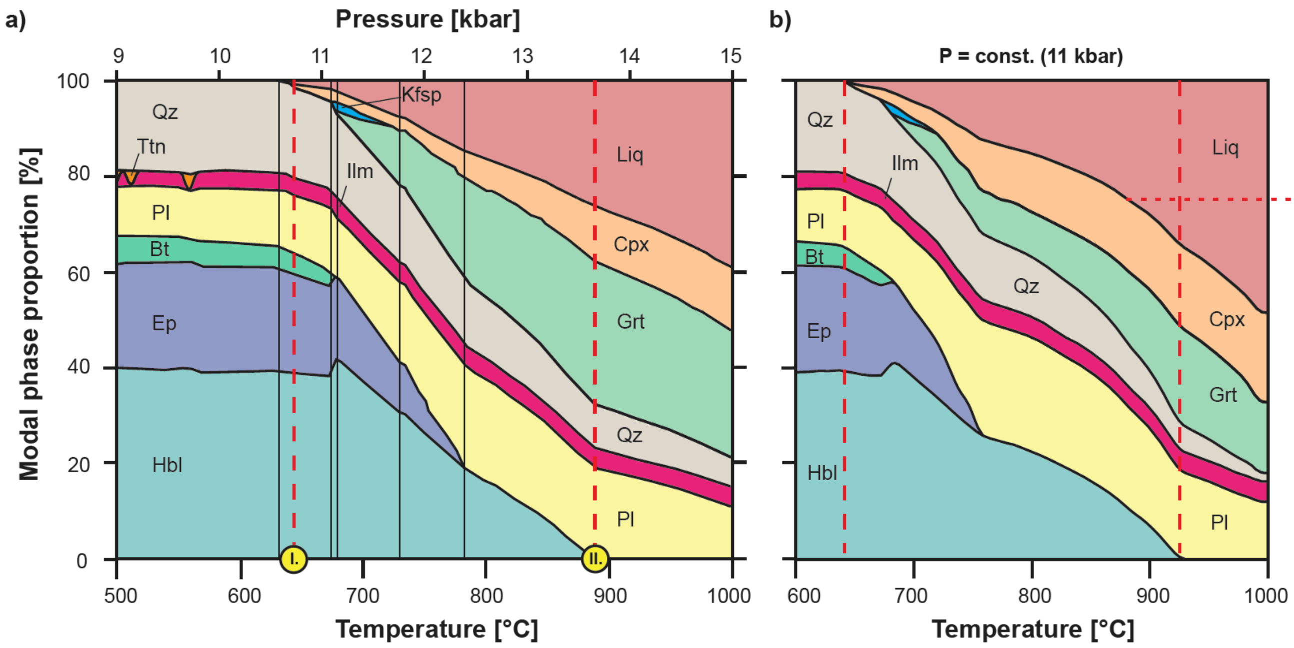

Supplementary Figure 8 | Modal phase proportions along the inferred partial melting P-T path. a, PerpleX computation of modal phase abundances along the inferred P-T path of 24°C km^{-1}, displayed in the pseudosection of Supplementary Fig. 7a. The vertical black lines indicate the appearance or disappearance of a specific phase; the red stippled lines mark the onset of partial melting (i) and the disappearance of hornblende (ii), respectively. The relative phase proportions indicate the de-hydration of epidote to form plagioclase between ca. 680-780°C, and the tonalitic partial melt producing reaction: hornblende + quartz + plagioclase = garnet + clinopyroxene + melt. Hornblende is fully consumed above ca. 890°C (ii), and melting continues through plagioclase consumption. Above the solidus, a decrease in minor biotite is observed, until its disappearance, marked by a slight increase in hornblende and the appearance of minor alkali-feldspar over a short temperature range. Thus, biotite is considered as a minor melt-entering phase in our trace element modelling (Methods). **b,** Computed modal phase abundances along an arbitrary isobaric (11 kbar) partial melting path for comparison. The chart demonstrates the presence of ca. 15% modal hornblende at proposed melt fractions of 25% (red horizontal stippled line; Methods). Abbreviations as in Supplementary Fig. 7.

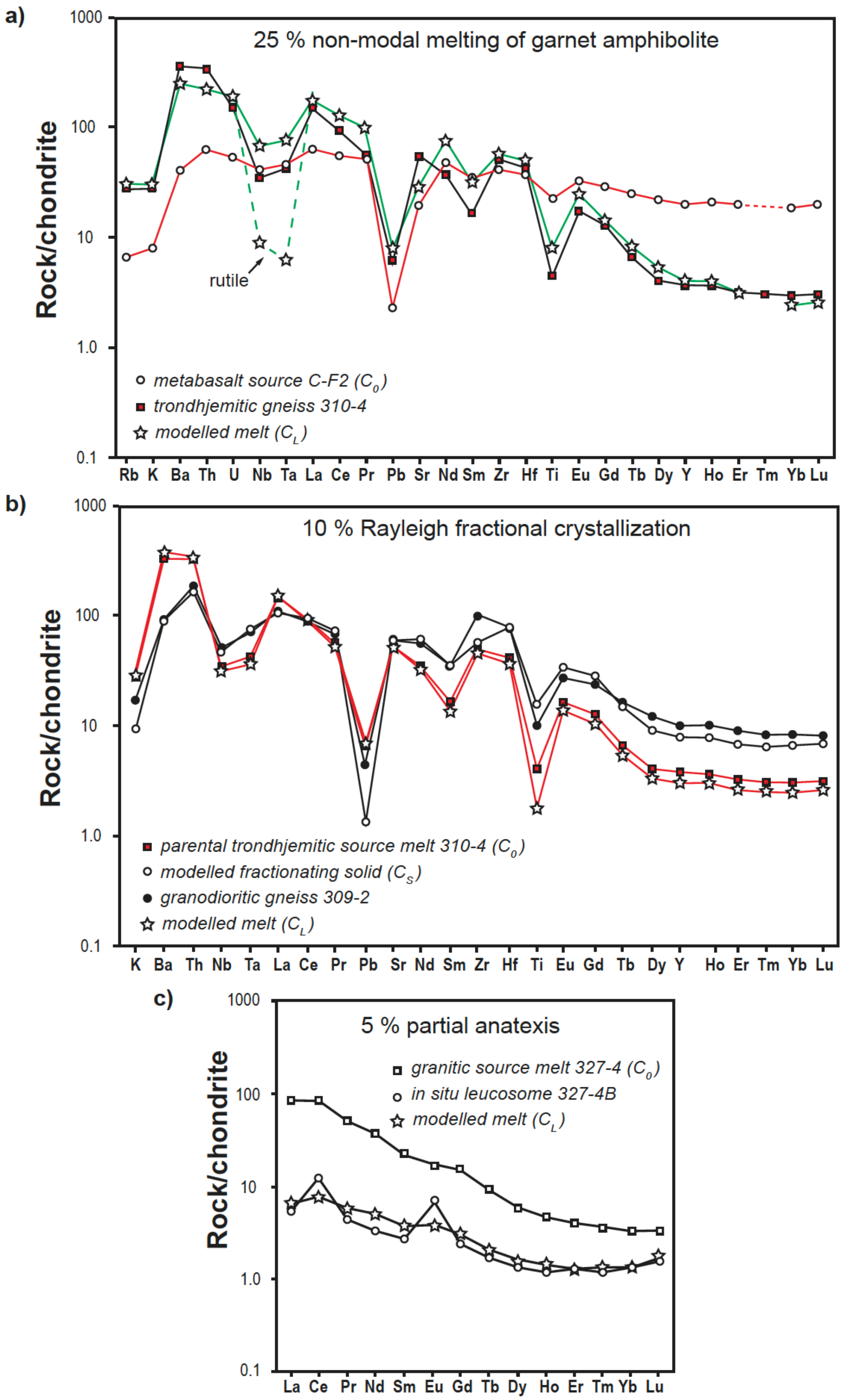
a)
25 % non-modal melting of garnet amphibolite
Rock/chondrite
1000
100
10
1.0
0.1
rutile
metabasalt source C-F2 (C_0)
trondhjemitic gneiss 310-4
modelled melt (C_L)
Rb K Ba Th U Nb Ta La Ce Pr Pb Sr Nd Sm Zr Hf Ti Eu Gd Tb Dy Y Ho Er Tm Yb Lu
b)
10 % Rayleigh fractional crystallization
Rock/chondrite
1000
100
10
1.0
0.1
parental trondhjemitic source melt 310-4 (C_0)
modelled fractionating solid (C_S)
granodioritic gneiss 309-2
modelled melt (C_L)
K Ba Th Nb Ta La Ce Pr Pb Sr Nd Sm Zr Hf Ti Eu Gd Tb Dy Y Ho Er Tm Yb Lu
c)
5 % partial anatexis
Rock/chondrite
1000
100
10
1.0
0.1
granitic source melt 327-4 (C_0)
in situ leucosome 327-4B
modelled melt (C_L)
La Ce Pr Nd Sm Eu Gd Tb Dy Ho Er Tm Yb Lu

Supplementary Figure 9 | Geochemical trace element modelling. Chondrite normalized spider-diagrams of selected trace elements (Chondrite values from McDonough, W.F., and Sun, S.-S. Composition of the Earth. *Chem. Geol.*, **120**, 223-253, 1995) for observed rock compositions and modelled melt (C_L) and residue (C_S) **a**, Using the putative TTG source metabasalt C-F2 (Supplementary Table 4; ref. 58), non-modal batch melting of garnet-amphibolite (40% hornblende-30% garnet-12% clinopyroxene-10% plagioclase-8% ilmenite) through 25% partial melting with a melt-entering modal phase abundance of 70% hornblende-20% plagioclase-10% biotite yields a modelled melt (C_L) that resembles the naturally observed trondhjemitic gneiss 310-4 composition. For comparison, mismatching variations in Nb-Ta are shown by using 8% rutile instead of ilmenite in the source, confirming our inferred P-T conditions for tonalitic melt production in absence of significant rutile (Supplementary Fig. 7a; Methods). **b**, 10% Rayleigh fractional crystallisation from a source melt, modelled as the naturally observed trondhjemitic gneiss 310-4, yields a fractionating solid composition that resembles the naturally observed granodioritic gneiss 309-2 (10% fractionation of 72% hornblende-10% plagioclase-10% ilmenite-5% titanite-1.5% rutile-1.3% apatite-0.2% zircon). **c**, Rare earth element spider-diagram of the naturally observed host granitic gneiss 327-4 (C_0), the spatially associated in situ leucosome 327-4B, and the modelled melt (C_L) through 5% non-modal partial melting. Partial melting (50% alkali feldspar-50% plagioclase as melt entering phases) was modelled using an initial solid of 45% plagioclase-24% biotite-15% apatite-10% titanite-5% alkali feldspar-1% allanite, consistent with the host rock mineralogy.